Article

Evaluating heat stress and occupational risks in the Southern Himalayas under current and future climates

Check for updates

Xiaoye Yang[1], Cheng Shen [1], Irfan Ullah [2], Julia Curio[1] & Deliang Chen [1,3] ✉

The southern Himalayas, characterized by its dense population and hot, humid summers, are confronted with some of the world's most severe heat stress risks. This study uses the hourly ERA5 dataset (1979–2022) and CMIP6 projections (2005–2100) to evaluate past and future heat stress based on the Wet Bulb Globe Temperature (WBGT). This has significant implications for the management of occupational workloads in the southern Himalayas. Heat stress levels are classified into 6 categories (0 to 5) using WBGT threshold intervals of 23 °C, 25 °C, 28 °C, 30 °C, and 33 °C. With heat stress surpassing level 3 for almost half of the time, people are constrained to engage in less than moderate workloads to ensure their health remains uncompromised. Flow-analogous algorithm is employed to contextualize the unprecedented heat stress case in the summer of 2020 and the associated atmospheric circulation patterns from historical and future perspectives. The results show that over 80% of the time in 2020, heat stress levels were at 3 and 4. The identified circulation pattern explains 27.6% of the extreme intensity, and such an extreme would have been nearly impossible in pre-21st-century climate conditions under the identified pattern. Future projections under SSP2-4.5 and SSP5-8.5 scenarios indicate that heat stress similar to what was experienced in 2020 will likely become a common occurrence across the southern Himalayas. Under a similar circulation pattern, the heat stress levels by the end of the 21st century would be elevated by at least one category compared to the climatic baseline in over 70% of the region, leading to an additional 120.5 (420.1) million daily population exposed to the highest heat stress level under the SSP2-4.5 (SSP5-8.5) scenario.

Over the last decade, global greenhouse gas concentrations have soared to unprecedented levels, resulting in a significant increase in the frequency, intensity, and persistence of extreme heat events worldwide[1,2]. These heightened temperatures can elevate core body temperature and heart rate, contributing to issues like heat-related illnesses, respiratory problems, cardiovascular diseases, and, in severe cases, fatalities[3–5]. The Southern Himalayas have emerged as a critical hotspot for extreme heat impacts, given their high population density, hot and wet climate, rapid urbanization, and limited adaptive capacity[6–12]. This makes the region highly susceptible to the influence of extreme weather conditions, particularly high temperatures[13–16].

A recent study reveals that between the years 2000 and 2019, over 5 million people worldwide died annually due to extreme temperatures, with approximately 2.6 million deaths occurring in Asia, predominantly in the Southern Himalayas[17]. In 2010, a heatwave in Ahmedabad, India alone resulted in the deaths of over 1300 individuals due to dehydration and heatstroke[18]. Another severe heatwave in June 2015 led to the death of 2500 people in Northern India, with temperatures reaching 49.4 °C in the border regions of Pakistan, causing 2000 fatalities[19,20]. In the aftermath of the extreme events in 2015, the National Disaster Management Authority in India designated heatwaves as a national-level disaster. By 2020, the frequency of heatwaves had surged, affecting 23 states in India, a notable increase from the initial impact on 9 states[21]. According to previous studies[14,22], if the global average temperature is restricted to 2 °C above preindustrial levels by the end of the 21st century, it is anticipated that the frequency and intensity of severe heat events in India will surge by 30 times. However, limiting global warming to 1.5 °C instead of 2 °C is projected to decrease the risk of the expected population in South Asia being exposed to dangerous extreme heat by nearly half[14]. It is imperative to address and mitigate these escalating climate-induced health risks to protect the well-being of the people.

[1]Department of Earth Sciences, Regional Climate Group, University of Gothenburg, Gothenburg, Sweden. [2]College of Hydrology and Water Resources, Hohai University, Nanjing, China. [3]Department of Earth System Sciences, Tsinghua University, Beijing, China. ✉e-mail: deliang@gvc.gu.se

Climate change not only increases temperature but also modifies humidity[23]. Theoretically, with every 1 °C rise in temperature, the atmospheric moisture content on average should increase by 7%[24,25]. While people can generally endure higher dry heat as the body cools through sweating, humid heat is more perilous[26,27]. A Wet Bulb Globe Temperature (WBGT) exceeding 30 °C poses a severe health risk for humans[28,29]. Excessive heat exposure places significant stress on the body, particularly affecting the cardiovascular system and potentially leading to heat-related disorders[30]. Children and the elderly are at the highest risk[31]. This is particularly evident in the Southern Himalayas, which heavily relies on outdoor agricultural labor[32,33]. The Southern Himalayas not only face the most severe heat stress globally under current climatic conditions but are also highlighted in the projections of the Sixth Phase of the Coupled Model Intercomparison Project (CMIP6), emphasizing the lethal heat stress risks at both daytime and nighttime it may encounter in the 21st century[34]. Studies consistently indicate that the sharp increase in GDP and population exposure to heat stress in this region is primarily attributed to climate change rather than population growth[34–38]. These findings underscore the pivotal role of climate change in shaping the significant risks associated with extreme heat conditions.

While previous studies have assessed summer heat stress in the region, examining both the current climate state and future climate changes, most of these investigations have not quantified the contribution of atmospheric circulation to extreme heat cases[22,37–39]. Moreover, most of the previous studies did not integrate heat stress risk levels associated with occupational workloads in the Southern Himalayas using WBGT. This omission leads to a less comprehensive understanding of its societal implications.

To address the two issues mentioned above, this study investigates the past and future heat stresses in the study region by utilizing a high spatio-temporal resolution ERA5 dataset[40] (hourly data with a horizontal resolution of 0.25° × 0.25°) and a state-of-the-art WBGT approximation method[41,42], together with a heat stress level classification related to workload recommendation. We also employ a flow-analogues algorithm[43,44] to comprehensively evaluate heat stress risk in the Southern Himalayas concerning atmospheric circulations. In this process, we quantify the contribution of atmospheric circulations to extreme heat stress and project the risk of future extreme heat stress under similar circulation patterns.

Results

Characteristics of heat stress in the Southern Himalayas

The terrain across the southern Himalayas (65–100°E, 20–35°N) is largely flat with intermittent transitional areas, and it hosts dense human settlements (Fig. 1a, b). This region has been subjected to the highest global risk of heat stress in recent decades (Fig. S1). The WBGT shows gradual declines from the northwest to the southeast across the southern Himalayas. Within this spectrum, Pakistan is exposed to the most severe heat stress risk, with its summer average WBGT reaching Category 3 and the maximum WBGT exceeding Category 5 (Fig. 1c, d). The summer average WBGT for Northern India, southern Nepal, and Bangladesh also attain Category 2, while the maximum WBGT reaches Category 4 (Fig. 1d, e). This represents a serious threat to outdoor agricultural production in the area[42,45].

Statistical results indicate that WBGT in Category 2 significantly prevails in the Southern Himalayas, constituting over 45.3% of the total hours across most regions (Fig. 2c). Moreover, the cumulative hours of WBGT falling within Categories 2 and 3 accounted for more than 22.6% and 13.6%, respectively, of the total hours in the northern sector of the Southern Himalayas (Fig. 2). This implies that, on average, the region experiences over 500 h of heat stress in Category 3 annually, more than 300 h of heat stress in Category 4, and 10 to 50 h of heat stress in Category 5 (with the highest in Pakistan facing over 500 h). Furthermore, the hours of heat stress in
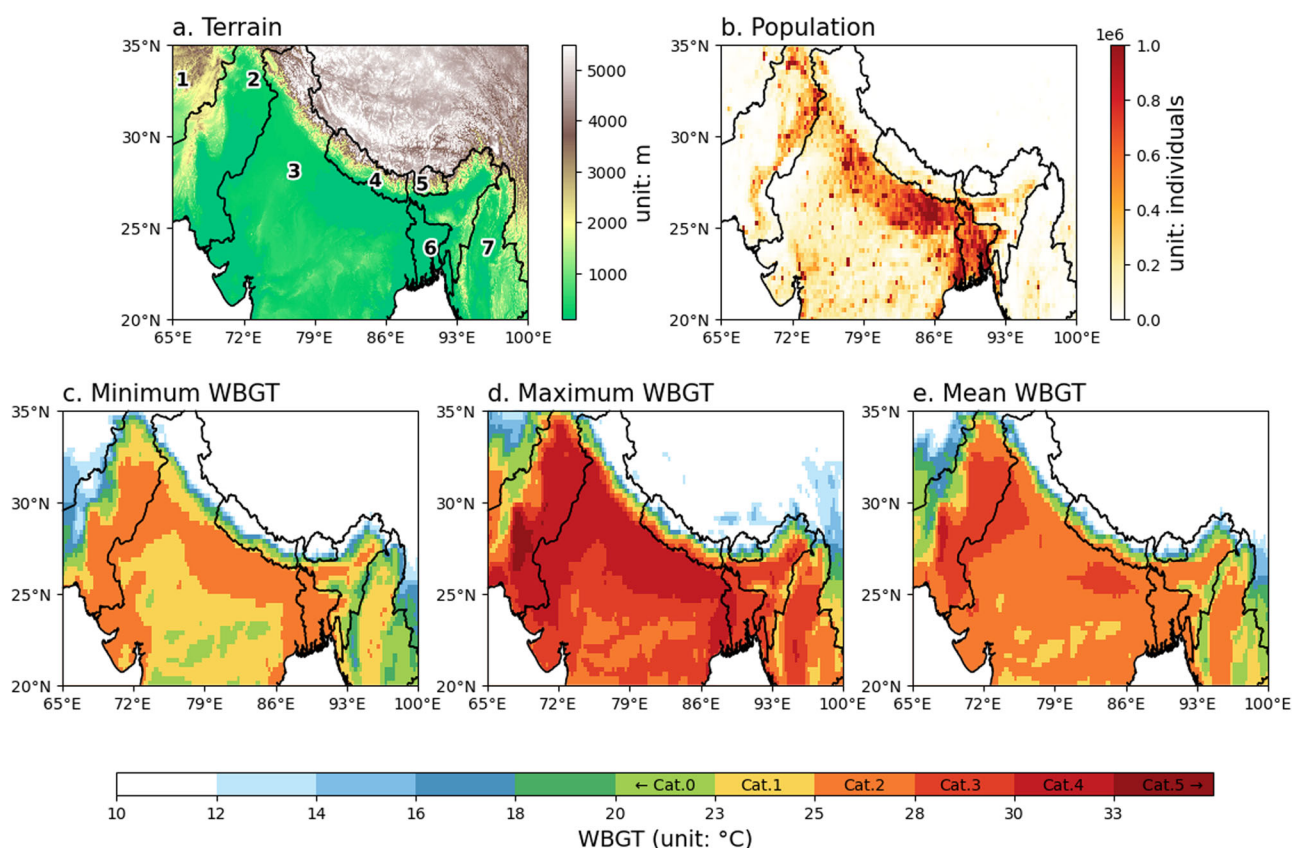

Fig. 1 | Topography, population, and WBGT in Southern Himalayas. a Southern Himalayas domain (shaded by elevation in units of meters) that includes 1: Afghanistan, 2: Pakistan; 3: India, 4: Nepal, 5: Bhutan, 6: Bangladesh, 7: Myanmar and (**b**) population (unit: 10[6] individuals) of the Southern Himalayas. Averaged (**c**) minimum, (**d**) maximum, and (**e**) mean summer WBGT from 1979 to 2022 (unit: °C).
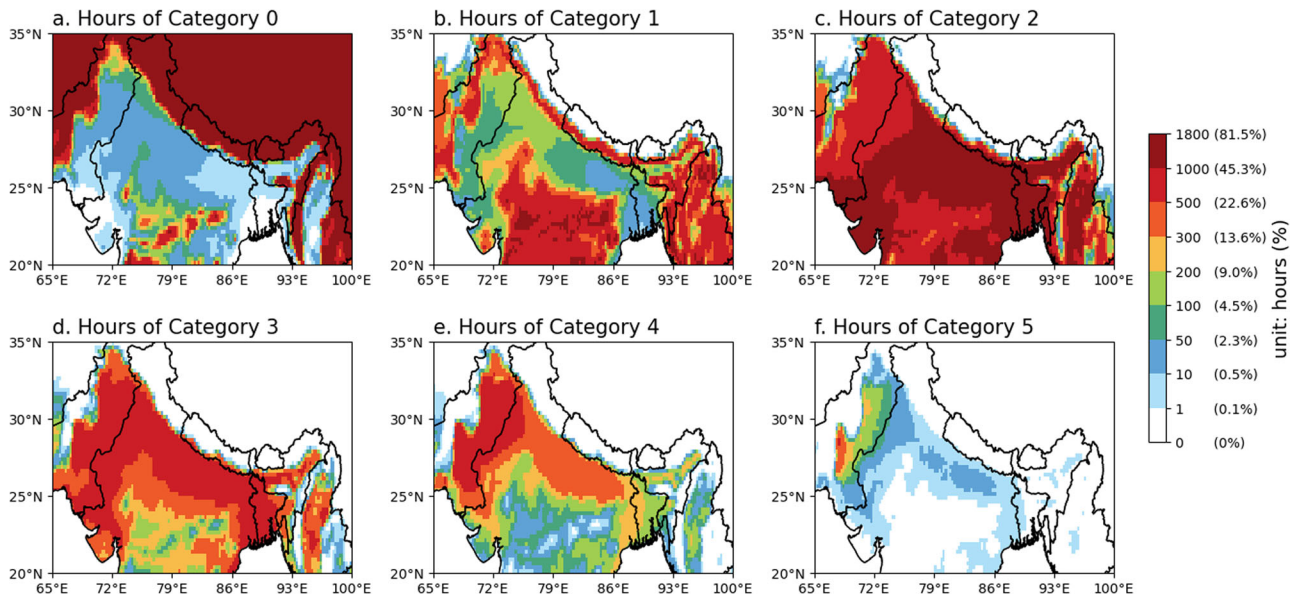
Fig. 2 | Summer heat stress within various categories in Southern Himalayas. Annual averaged hours of summer heat stress from 1979 to 2022 in Category (**a**) 0, (**b**) 1, (**c**) 2, (**d**) 3, (**e**) 4, and (**f**) 5.
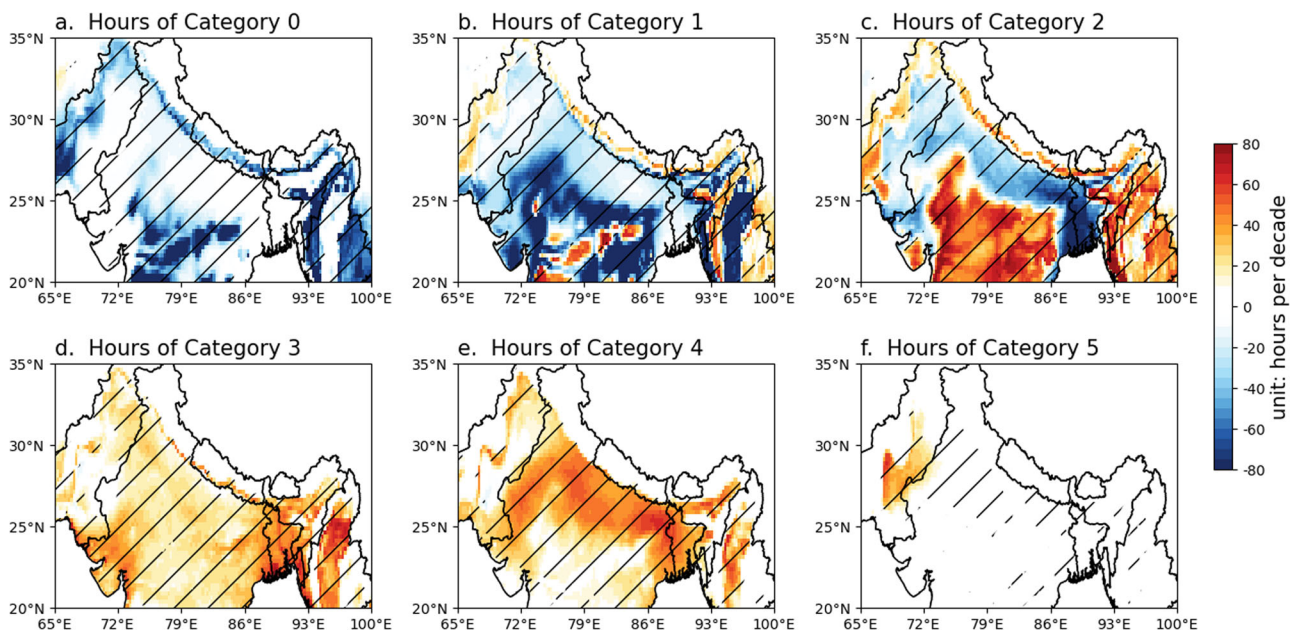

Fig. 3 | The trend of heat stress hours in Southern Himalayas. The trend of summer heat stress hours from 1979 to 2022 in Category (**a**) 0, (**b**) 1, (**c**) 2, (**d**) 3, (**e**) 4, and (**f**) 5 (unit: hours per decade; regions marked with lines have undergone a significance test at the 0.05 level).

Categories 3–5 show a strong rising trend (Fig. 3). There is a consistent increase in the number of heat stress hours in Categories 3 to 5 in the southern Himalayas. The most significant rise is noted in Category 4, showing an increase of ~40–60 h per decade (Fig. 3e). Consequently, the window of comfortable climate conditions is notably shortened (Fig. 3a–c).

Atmospheric circulation of the record-breaking extreme heat stress in Summer 2020

The escalating trend of heat stress risks in the southern Himalayas has intensified in recent decades, exhibiting a non-linear growth trend (Fig. 4a). Particularly in recent years, the regional annual average WBGT has hovered around 20 °C, with the highest WBGT recorded in 2020. During the summer of 2020, nearly every day saw WBGT surpassing historical averages for the same period. Notably, the period between July 24th and August 16th

witnessed the maximum WBGT in over four decades (Fig. 4b). Moreover, the WBGT for the rest of the days also exceeded the 90th percentile threshold. Whether assessed through individual synoptic-scale case analyses or from the perspective of long-term climate conditions, this extreme heat stress closely correlated with anomalies in localized surface low-pressure systems (Fig. 5). The low-pressure anomaly could lead to a reduction in total cloud cover over the southern Himalayas, allowing more solar radiation to heat the surface air (Fig. S2a, b). Positioned north of the cyclone center, the southern Himalayas are influenced by the southwestern airflow from the Arabian Sea. This airflow could bring warm and humid conditions, contributing to the maintenance of high WBGT levels (Fig. S2c).

Figure 6a–c specifically display the distribution of heat stress hours during the period from July 24th to August 16th, 2020. Most areas predominantly experienced heat stress in Categories 3 and 4, accumulating over
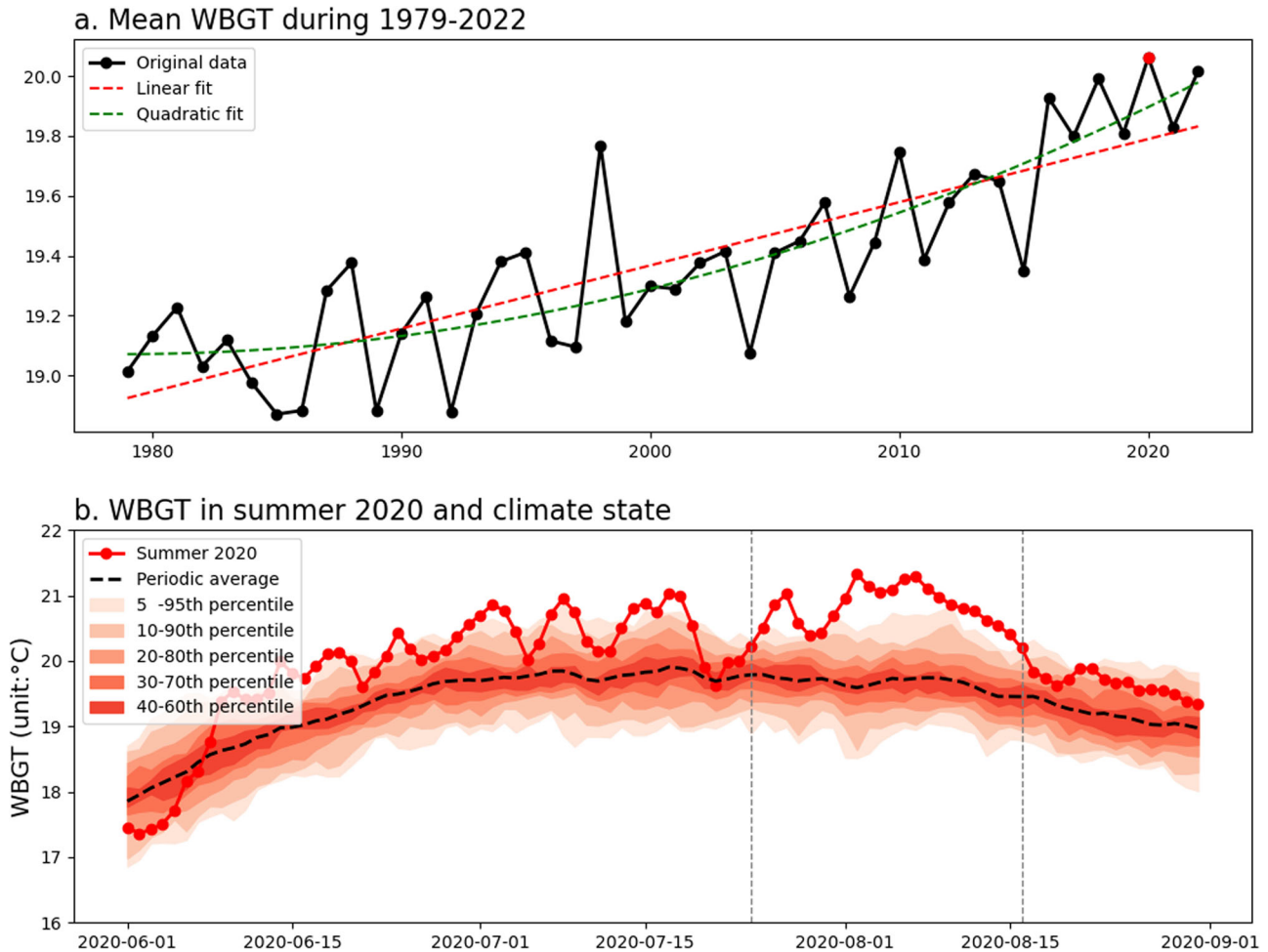
Fig. 4 | Record-breaking heat stress extreme in summer 2020. a Mean summer WBGT in the Southern Himalayas with its linear trend and non-linear trend. **b** Daily mean WBGT in summer 2020 and contemporaneous climatological level during 1979–2022.
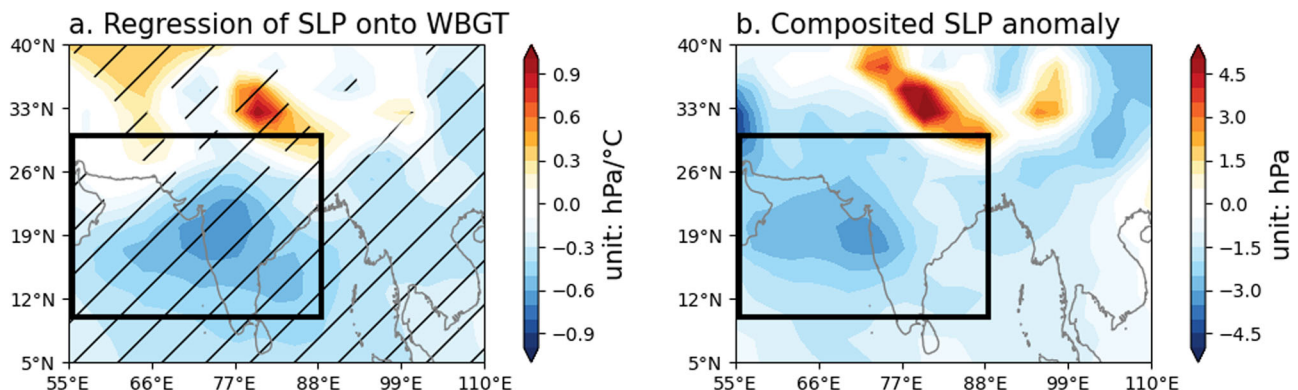

Fig. 5 | Local circulation anomalies related to heat stress in Southern Himalayas. a The linear regression of sea level pressure (SLP) onto WBGT in the southern Himalayas (unit: hPa/°C; regions marked with lines have undergone a significance test at the 0.05 level). **b** Composited surface pressure anomalies during July 24th and August 16th in 2020 (unit: hPa). The black box (55–88°E, 10–30°N) denotes the domain size of the analogues.

50% of the hours. This suggests that people working outdoors were limited to engaging in moderate or light workloads throughout most of the day, and even at night, obtaining quality rest was challenging due to excessive heat. Especially in certain regions of Pakistan, heat stress in Category 5 accounted for approximately 30% of the entire day. A further comparison between the reconstructed average WBGT in the southern Himalayas based on the Flow Analogues algorithm and the observed results (Fig. 6d) suggests that, between 1979 and 2022 (excluding 2020), comparable circulation patterns rarely resulted in such an extreme heat stress case. Over the 24 days from

July 24th to August 16th, only 13 days of WBGT records aligned with similar circulation conditions. The atmospheric circulation contributed only 27.6% to this extreme heat stress case according to the assessment method outlined in section of Method (the observed WBGT anomaly stood at 1.2 °C, whereas the reconstructed average anomaly was a mere 0.3 °C).

Contribution of present and future climate change to heat stress
The findings from Fig. 6 suggest that atmospheric circulation accounts for only a small portion of this extreme heat stress. To further assess the impact
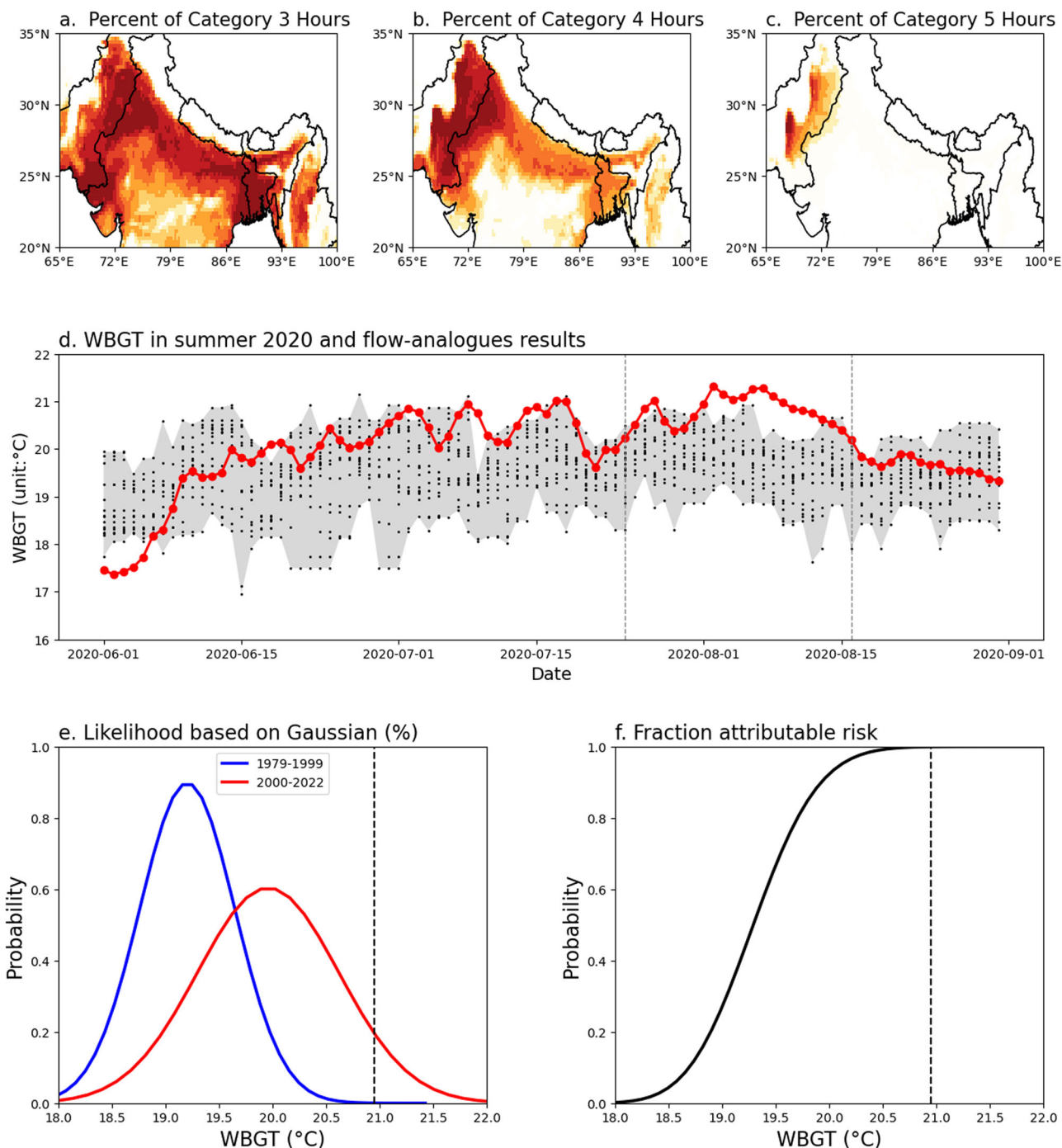
Fig. 6 | Distribution of heat stress extreme in summer 2020 and the contribution of climate change. Percentage of hours in Category (**a**) 3, (**b**) 4, and (**c**) 5 during July 24th and August 16th in 2020 (unit: %). **d** Daily mean WBGT in summer 2020 (red line) and the reconstructed WBGT via Flow Analogues algorithm (black dots within the gray band). **e** Gaussian probability density distributions fitted to reconstructed WBGT via Flow Analogues algorithm. The blue line denotes the WBGT in the past climate (1979–1999) and the red line denotes the present climate (2000–2022). **f** Attributable fraction of climate change for WBGT. The dotted lines denote the observed average WBGT from July 24th to August 16th in 2020.

of climate change on this case, the algorithm was separately applied to historical and current climate samples, with the obtained results fitted to a normal distribution (Fig. 6e). Under historical climatic conditions, a similar circulation pattern would have resulted in an average WBGT of 19.2 °C, making it highly unlikely to trigger this extreme heat stress event (probability less than 0.1%). However, under the current climatic conditions, a similar circulation pattern would yield an average WBGT of 19.9 °C, with a 9.9% probability of reaching the WBGT levels observed during the extreme heat stress case in 2020. The attributable fraction for the WBGT during this

extreme heat stress case approached 1.0 (Fig. 6f), underscoring the impact of climate change. This extreme event would not have occurred without its influence.

The identified similar circulation patterns in the CMIP6 simulations effectively replicated the cyclonic circulation anomaly center with almost the same intensity over the west coast of India (Fig. S3) and showed an excessive capture of positive SLP anomalies in northeast India. Overall, the spatial correlation coefficients ranged between 0.48 and 0.49 when compared to observational data. Figure 7 displays the daily mean WBGT in future
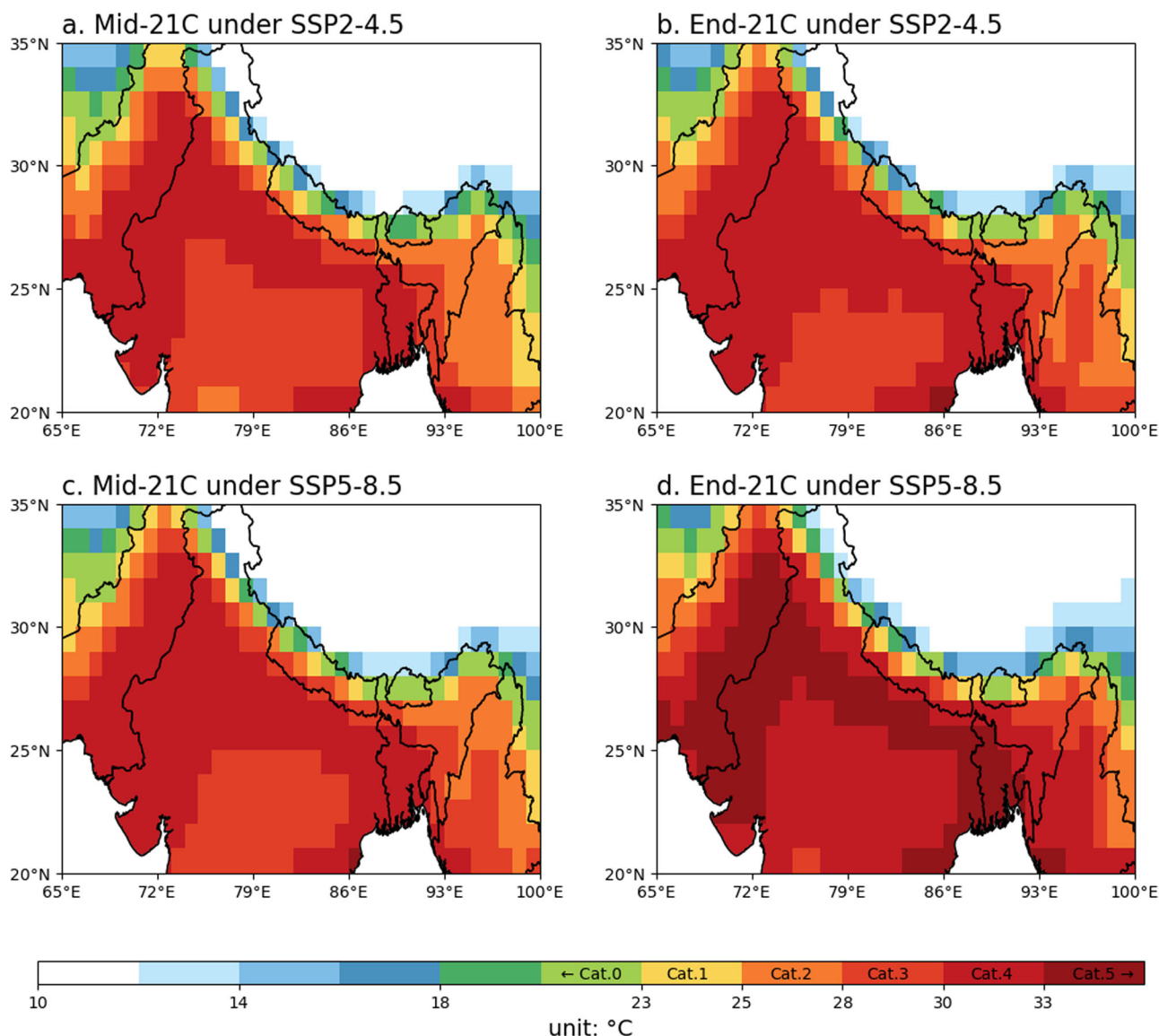
Fig. 7 | Heat stress risk in the 21st century in Southern Himalayas. Multi-model ensemble mean WBGT (unit: °C) of 15 best similar circulation patterns during (**a**, **c**) 2040–2060 and (**b**, **d**) 2080–2100 under SSP2-4.5 (**a**, **b**) and 2040–2060 and 2080–2100 under SSP5-8.5 (**c**, **d**).

climates under similar circulation patterns and intensity. A noticeable warming is observed in the southern Himalayas compared to the early 21st century. By the mid-21st century, the daily average WBGT in the plains of the Southern Himalayas consistently exceeds 28 °C. Regions like Pakistan, northwestern India, and Bangladesh experience daily average WBGT surpassing 30 °C, placing these areas under severe heat stress categorized as Category 3. By the end-21st century, the distribution of daily average WBGT under the SSP2-4.5 scenario closely resembles the levels observed in the mid-21st century under SSP5-8.5. However, under SSP5-8.5 by the end of the century, the daily average WBGT in the plains of the southern Himalayas consistently exceeds 30 °C, with some areas surpassing 33 °C. This implies that people in these regions would find it nearly impossible to engage in any outdoor labor throughout the day.

The multi-model ensemble WBGT in the Southern Himalayas estimated from CMIP6 historical simulations is slightly higher than the results obtained from ERA5 with a deviation within 5% (less than 0.5 °C as shown in Fig. 8a), which may be attributed to the absence of daily radiation data in the approximation. The significant divergence in WBGT between the SSP2-4.5 and SSP5-8.5 scenarios becomes pronounced from the mid-21st century. By the end-21st century, the WBGT under the SSP2-4.5 scenario remains below 22 °C, whereas under the SSP5-8.5 scenario, it reaches a high of 24 °C.

This implies that, regardless of the scenario, the climate state by the end-21st century is expected to surpass the extreme cases observed in the summer of 2020. The error bars in Fig. 8a provide a clear contrast between the summer averaged WBGT and reconstructed WBGT via the Flow-analogues algorithm during the mid-21st century and the end-21st century. The reconstructed WBGT notably surpasses climatological levels, particularly in the end-21st century. This implies that, within the context of a warming climate, the cyclonic anomalies can further enhance heat stress in the southern Himalayas. The projected WBGT in the southern Himalayas, reconstructed using the flow-analogues algorithm, is anticipated to reach 23.4 °C (under SSP2-4.5) and 25.3 °C (under SSP5-8.5) by the end-21st century (Fig. 8b). The calculations show that this is 1.5 °C (SSP2-4.5) and 1.3 °C (SSP5-8.5) higher than the summer averaged WBGT during the same period, and 2.6 °C (SSP2-4.5) and 4.5 °C (SSP5-8.5) higher than the WBGT observed during the extreme cases in the summer of 2020 (with an average WBGT of 20.8 °C from July 24th to August 16th, 2020). In contrast, the reconstructed WBGT in the end-21st century exhibits a larger uncertainty range under the SSP585 scenario due to its higher variance.

Finally, the changes in heat stress levels under similar circulation patterns in the southern Himalayas region for the future are quantified (Fig. 9). Compared to the summer average heat stress levels during the same
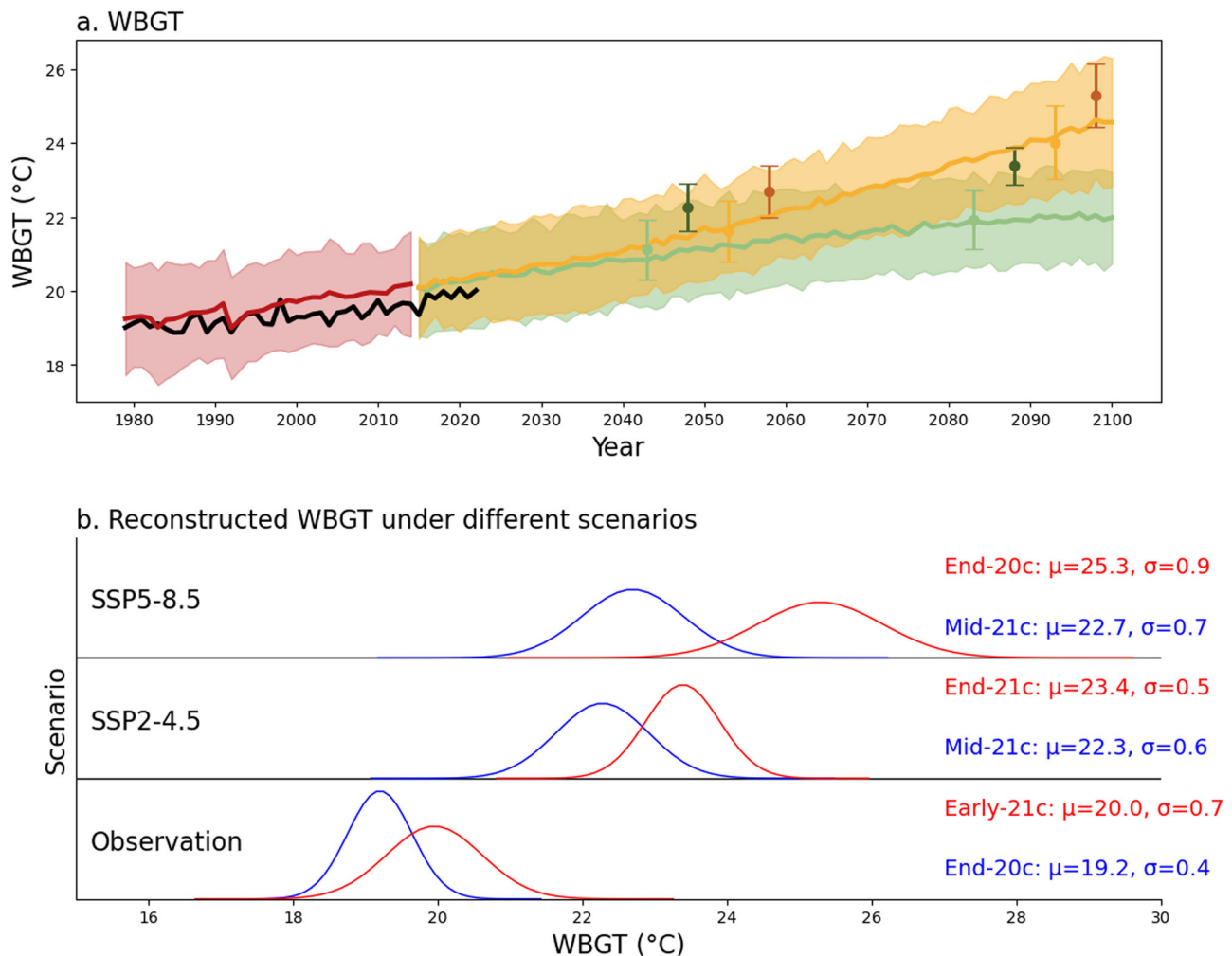
Fig. 8 | Projected WBGT and reconstructed WBGT in the Southern Himalayas in the 21st century. a Observed (black line) and CMIP6 simulated WBGT (red line for historical simulation, green line, and yellow line for SSP2-4.5 and SSP5-8.5 scenario, respectively) in the 21st century. The shading bands are 1.5 times the standard deviation among the models. Error bars denote the mean climatic WBGT (with a lighter color) and reconstructed WBGT obtained from analogues algorithm (with a darker color) in the mid-21st century and end-21st century. **b** Gaussian distributions fitted to reconstructed WBGT via Flow Analogues algorithm under different scenarios.

period (Fig. S4), under the influence of cyclonic anomalies, the heat stress levels in approximately a quarter of the southern Himalayan region would have increased by at least one level. About 3–4% (Less than 2%) of the area would see a 2-level (3-level) increase in heat stress levels. Results for different scenarios in the mid-and end-21st century are similar, indicating that the contribution of atmospheric circulations to extreme heat stress would have almost not changed with the variation in climate states. In comparison to the extreme case in the summer of 2020, controlled by similar circulation patterns, it is apparent that by the mid-21st century under SSP2-4.5 (SSP5-8.5), the southern Himalayas is expected to witness a 1-level increase in extreme heat stress for 32.3% (36.8%) of the region and a 2-level increase for 7.0% (8.8%) of the region. The divergence between the moderate-emission and high-emission scenarios is primarily evident in the end-21st century. Under SSP2-4.5 (SSP5-8.5), 36.8% (30.3%) of the southern Himalayas is projected to experience a 1-level increase in heat stress, while 15.0% (38.0%) of the area would see a two-level increase, and 1.6% (7.4%) of the region will witness a 3-level increase in heat stress. This implies that in the most densely populated areas of the southern Himalayas, the daily average WBGT is expected to consistently remain at heat stress levels of 5 throughout the day under the SSP5-8.5 by the end of the 21st century.

The statistical calculations on population exposure to heat stress in level 4 and 5 indicate a significant increase by the end of the 21st century compared to the historical period under the identified circulation pattern

(Fig. 9c, d). Specifically, under the SSP2-4.5 (SSP5-8.5) scenario, there would be an additional 646.5 (451.3) million people exposed to level 4 heat stress and 120.5 (420.1) million people exposed to level 5 heat stress daily, respectively (Fig. 9c). Towards the end of the 21st century, the projected daily population exposed to heat stress under identified circulation conditions is also notably higher compared to the climatic level in the same period (Fig. 9d). Under the SSP2-4.5 scenario, the number of individuals exposed to level 4 and 5 heat stress increases by 51.2 million and 41.4 million, respectively. Under the SSP5-8.5 scenario, the projected population exposed to level 5 heat stress rises by 36.7 million, primarily attributed to an excessive warming, leading to the summer average WBGT nearing critical levels by the century's end. In this context, population growth contributes only 18.2% ± 5.1% (6.5% ± 0.9%) to the increase in population exposure to heat stress under the SSP2-4.5 (SSP5-8.5) scenario, which indicates that climate factors play a more critical role. Such results highlight the critical necessity for implementing adaptive strategies and mitigation measures to tackle the escalating heat stress in the southern Himalayas.

Discussion

This study assesses summer WBGT over the southern Himalayas using the Brimicombe approximation[41]. The region faces some of the world's most severe heat stress risks. Many areas in the region consistently experience Level 3 heat stress (WBGT exceeding 28 °C) for nearly half of the summer
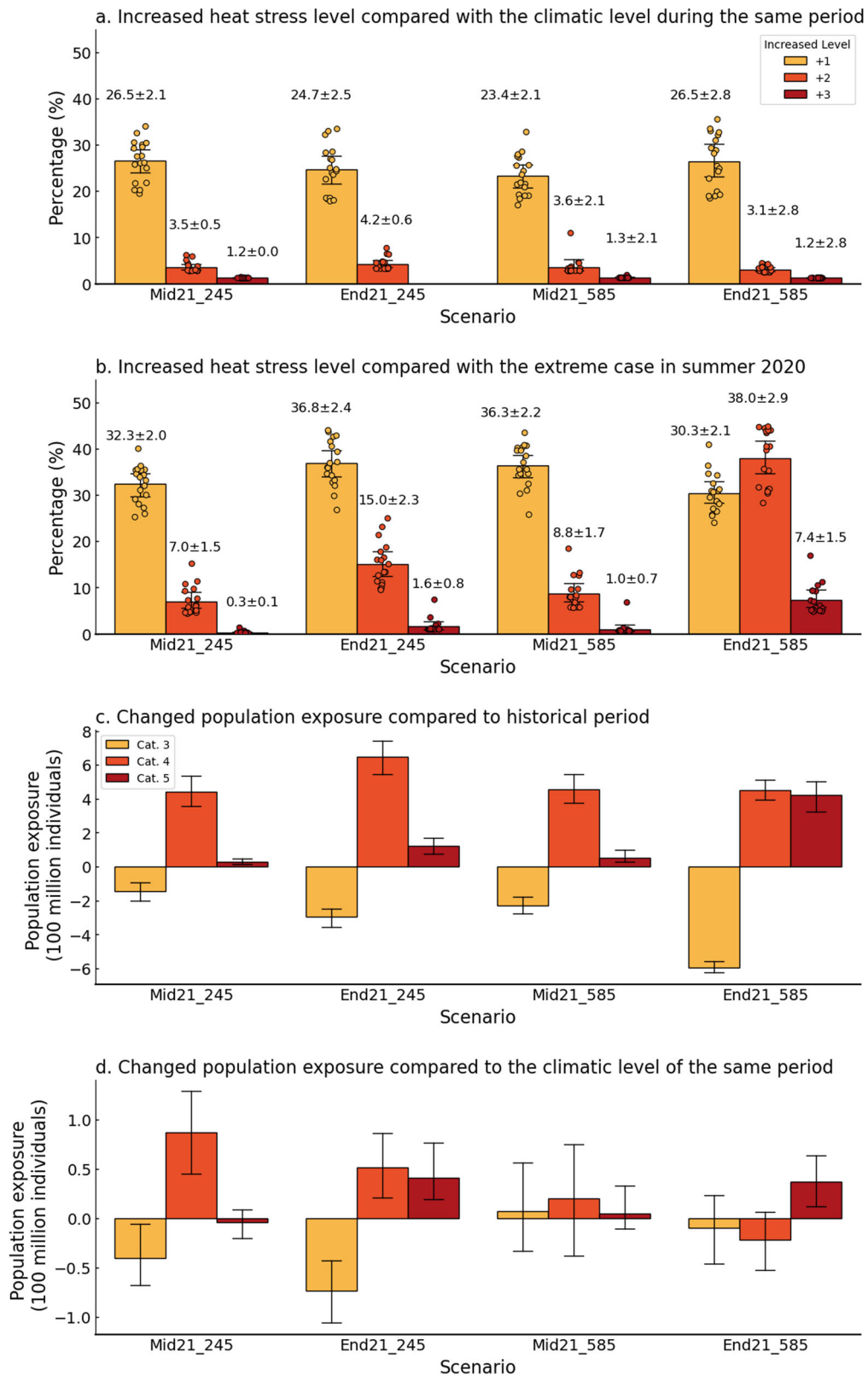
Fig. 9 | Impact of climate conditions and local circulation anomalies on heat stress risk. a The percentage of area in the southern Himalayas where the heat stress level has increased by at least 1 level compared to the climate statement in the same period. **b** The percentage of area in the southern Himalayas where the heat stress level has increased by 1, 2, and 3 levels compared to the extreme case in the summer of 2020. The error bars mark the 95% confidence interval, and the scatter points are the results of each of the 18 models. **c** Differences in daily population exposed to heat stress caused by identified circulation pattern under different scenarios and daily population exposed to heat stress in the historical period. **d** Differences in daily population exposed to heat stress caused by identified circulation pattern under different scenarios and summer averaged daily population exposed to heat stress in the same period.

hours, restricting people to engage only in outdoor work of moderate or lower intensity during these periods.

WBGT in this region has exhibited a nonlinear growth trend in recent years, particularly evident during the record-breaking extreme heat stress event in the summer of 2020. This extreme heat stress event was strongly associated with the local surface low-pressure system anomaly. The application of flow-analogues algorithms, based on the circulation patterns associated with the 2020 event, indicates that atmospheric circulation contributed 27.6% to the intensity of this event, and the occurrence of such an extreme event was nearly implausible under climate conditions before the 21st century.

Projected results indicate that, under both moderate and high emission scenarios, the summer average WBGT in the southern Himalayas by the end of the 21st century would surpass the extreme heat stress event observed in the summer of 2020. Under the control of circulation patterns similar to those during the extreme heat stress event of 2020, the heat stress levels across more than half of the southern Himalayas are projected to significantly increase by at least one level compared to the extreme event in 2020. The evident influence of climate change on extreme heat stress events underscores the significance of worldwide initiatives aimed at reducing emissions and constraining additional temperature rises.

The major limitation of this study arises from the use of the flow-analogues algorithm. Since the extreme case in 2020 was a record-breaking event, finding exact matches with similar circulation patterns proves challenging, resulting in reconstructed outcomes that are lower than the actual levels[46]. Furthermore, it is crucial to highlight that, due to limitations stemming from the lack of daily radiation data in estimating WBGT in CMIP6, the projected WBGT slightly (less than 5%) overestimates the heat stress risks in the southern Himalayas, offsetting the adverse effects of the algorithm to a certain extent. Considering that WBGT is influenced by multiple factors, including temperature, humidity, wind speed, and radiation, future research should aim to assess more specifically the relative contributions of these components. Finally, due to the limited observational data time span, future studies could explore the relative roles of external forcing and internal climate variability over a longer time scale through large-member simulations. In conclusion, interdisciplinary collaboration is essential to quantify the concrete impacts of climate change, which are pivotal for strategic planning and climate adaptation efforts.

Methods
Data
This study used the hourly ERA5 reanalysis dataset from 1979 to 2022 with a horizontal resolution of $0.25° \times 0.25°$[40]. The 2-m air temperature, 10-m wind speed, and mean radiant temperature from ERA5 were used to calculate the WBGT, while the geopotential height and surface pressure were used to analyze the corresponding circulation conditions.

To project future changes in heat stress, simulations from 18 models in the CMIP6 archives, due to the availability of daily surface air temperature and humidity data, were used[47]. Supporting Information of Table S1 lists the basic information of these models. The historical simulations (1979–2014) and future projections (2015–2100) were analyzed under two major emission scenarios: SSP2-4.5 (mid-emission pathway) and SSP5-8.5 (high-emission pathway). SSP5-8.5 incorporates the SSP5 scenario, characterized by emissions sufficient to yield a radiative forcing of 8.5 W·m⁻² by the year 2100. While SSP2-4.5 combines intermediate societal vulnerability (SSP2) with a moderate radiative forcing of 4.5 W·m⁻². Furthermore, only the first realization of each model was selected for the analysis. All CMIP6 simulations are bilinearly interpolated to a $1° \times 1°$ horizontal resolution.

The past (2000–2020) and projected (2010–2100) population datasets are obtained from WorldPop (DOI: 10.5258/SOTON/WP00647) and version 1 of Global 1-km Downscaled Population Projection Grids for the SSPs[48].

WBGT approximation and the heat stress level
The WBGT is a metric extensively utilized in the fields of occupational and public health research. It has also gained popularity as a key heat stress measure in climate change studies[32,33,36]. The WBGT, measured in degrees Celsius (°C), is computed based on three environmental elements, as outlined by Minard in 1961:

$$WBGT = 0.7T_W + 0.2T_g + 0.1T_a \qquad (1)$$

where T_W is natural wet bulb temperature, T_g is globe thermometer temperature, and T_a denotes the surface air temperature at 2 m, all three components are in the unit of °C. The surface air temperature is easy to record, while observational records of globe thermometer and wet bulb thermometer temperatures are scarce. Consequently, WBGT is usually obtained through approximation operations in previous studies[49,50].

A recent study introduced a novel approximation method for WBGT[41]. Compared to previous approaches, this method yields results closer to observational levels, is applicable across a wider spatial range, and can be easily calculated using meteorological elements from ERA5 reanalysis data.

In this approximation, the globe temperature is solved by the following equation:

$$T_{MRT} = \sqrt[4]{T_g^4 + \frac{h_{cg}}{\varepsilon \times D^{0.4}} \times (T_g - T_a)} \qquad (2)$$

Where $h_{cg} = 1.1 \times 10^8 \times v_a^{0.6}$ denotes the mean convection coefficient and v_a represents the 10-m wind speed. T_{MRT} is the mean radiant temperature, which can be obtained from ERA5 reanalysis.

The theoretical method used to calculate the T_W is the same as the previous study[51]:

$$\begin{aligned} T_W = {} & T_a \tan^{-1}\left(0.151977(RH + 8.313659)^{\frac{1}{2}}\right) + \tan^{-1}(T_a + RH) \\ & - \tan^{-1}(RH - 1.676331) + 0.00391838(RH)^{\frac{3}{2}} \\ & \times \tan^{-1}(RH \times 0.023101) - 4.686035 \end{aligned} \qquad (3)$$

When T_W and T_g are solved, WBGT can be estimated by Eq. (1).

Given the unavailability of daily radiation data in CMIP6 simulations, only a simple estimate of WBGT can be derived using surface air temperature and humidity[49]. This simplified approximation does not account for variations in solar radiation intensity or wind speed, and it presumes a moderately high radiation level under light wind conditions. Consequently, it may result in an overestimation of the WBGT by approximately 1–2 °C in cloudy and windy conditions[52].

Table S2 presents the heat stress thresholds for WBGT and the suggested workloads[42]. This study focuses on heat stress with Category 3 (28–30 °C), 4 (30–33 °C), and 5 (>33 °C), as they correspond to the maximum workloads of moderate, light, and resting, respectively. The establishment of these thresholds facilitates assessment of societal risks associated with heat stress, thereby enhancing the relevance of this study for people's living conditions in the region.

Flow-analogues algorithm
To quantify the contribution of atmospheric circulation conditions to the formation of extreme heat stress in different climate states, a flow-analogues algorithm is employed. The fundamental concept of this algorithm involves identifying historical circulation patterns that are associated with the specified case, comparing disparities in meteorological elements under these similar circulation patterns in different periods, and assessing the contribution of the determined circulation conditions to this extreme case[43,44,46,53,54]. A schematic flowchart of the algorithm is provided in Fig. S5.

Specifically, the detailed steps are as follows: (1) Calculate the spatial correlation coefficient of sea level pressure (SLP) in the region of (55–88°E,

10–30°N; derived from Fig. 5) between each day and the days during the extreme case, and then select the 15 most similar analogs for each day. (2) For each day, one of these 15 analogs is randomly picked, allowing the corresponding variables to be reconstructed into a new sequence. (3) To obtain robust results, the simulation process is repeated 100,000 times. As the number of simulations increases, the results tend to follow a normal distribution following the Central Limit Theorem (Kwak and Kim, 2017). To eliminate the influence of seasonal cycles, the similar circulation patterns identified for a given day are selected from samples spanning 43 years × 61 days (excluding circulations in the same year as the focused case) centered around that day, with 30 days before and after. The Flow-analogues algorithm in "Atmospheric circulation of the record-breaking extreme heat stress in Summer 2020" utilized detrended SLP and WBGT data, removing the quadratic trend fittings to mitigate the impact of climate change. Conversely, in "Contribution of present and future climate change to heat stress", the trend was retained to detect differences between the two sets of climates[44,46]. For removing the trend form the original data $y(t)$, t represents time. First, perform a quadratic polynomial fit to the data: $\hat{y}(t) = at^2 + bt + c$, Here, $\hat{y}(t)$ is the quadratic fit, and a, b, c are the fitting coefficients. Then, subtract this quadratic fit from the original data to obtain the detrended data $\bar{y}(t) = y(t) - \hat{y}(t)$.

Flow-analogues algorithm relies on four crucial choices: the number of similar circulation patterns obtained, the approach to evaluate spatial similarity in circulation, the meteorological variable to represent circulation patterns, and the size of the circulation domain. To obtain robust results, a sensitivity test of these four settings is compared (Fig. S6). The effectiveness of the algorithm is indicated by how closely the outcomes derived from similar circulation patterns align with observed results (the smaller the standard deviation and the closer the mean to observed outcomes, the higher the performance of the algorithm). Based on this algorithm, we can determine the contribution of local circulation patterns to the specified intensity of extreme heat stress case, rather than the contribution of one meteorological element. In this study, we use SLP to represent local circulation patterns.

Assessing the influence of climate change on extreme events

The contribution of atmospheric circulation can be quantified by dividing the difference between the mean simulated anomalies and the observed anomaly. To assess the impact of climate change, we adopted the methodologies like the previous studies[44,46]. In the historical period (1979–2022), the data are categorized into two groups: the historical climate (1979–1999) and the current climate (2000–2020). In the CMIP6 simulations, the projected results for the near future (2040–2060) and far future (2080–2100) are selected. These four groups of data represent the climate states of the historical, present, mid-21st century, and end-21st century, respectively. After fitting normal distributions to the simulated results of the two sample groups, the probability of extreme events exceeding a specified threshold can be estimated. Consequently, the influence of climate change on the likelihood of extreme events can be quantified by the Attributable Fraction, defined as:

$$Attributable\ Fraction = \frac{P_b - P_a}{P_b} \qquad (4)$$

here P_a and P_b represent the occurrence likelihood in any two of the historical, current, near future, or far future climate groups. The closer the result is to 1, the stronger the impact of climate change.

Assessing the exposure of population to heat stress

This study used the population exposed to heat stress to describe its exposure, like previous studies[55–57]. The exposure is dependent on the heat stress and population, implying that the exposure will increase when the heat stress days occur, or the population rises. The calculation is as follows:

$$Exposure_{population} = population \times heat\ stress\ days \qquad (5)$$

based on this equation, we can determine the number of people exposed to each level of heat stress, as well as the relative contributions of population growth and the increase in heat stress days.

Data availability

The data used in this study are publicly available. ERA5 reanalysis dataset is available in this in-text data citation reference: Hersbach et al.[40]; The CMIP6 simulations can be obtained from https://esgf-node.llnl.gov/projects/cmip6/.

Code availability

The source codes for the analysis of this study are available from the corresponding author upon reasonable request.

References

1. Masson-Delmotte, V. et al. *Climate change 2021: the physical science basis*. *Contribution of working group I to the sixth assessment report of the intergovernmental panel on climate change*. (University Press, 2021).
2. Luo, M. et al. Anthropogenic forcing has increased the risk of longer-traveling and slower-moving large contiguous heatwaves. *Sci. Adv.* **10**, eadl1598 (2024).
3. Dematte, J. E. et al. Near-fatal heat stroke during the 1995 heat wave in Chicago. *Ann. Intern. Med.* **129**, 173–181 (1998).
4. Xing, Q. et al. Impacts of urbanization on the temperature-cardiovascular mortality relationship in Beijing, China. *Environ. Res.* **191**, 110234 (2020).
5. Yang, J. et al. Projecting heat-related excess mortality under climate change scenarios in China. *Nat. Commun.* **12**, 1039 (2021).
6. ul Hassan, W., Nayak, M. A. & Lyngwa, R. V. Recent changes in heatwaves and maximum temperatures over a complex terrain in the Himalayas. *Sci. Total Environ.* **794**, 148706 (2021).
7. Singh, S., Mall, R. K. & Singh, N. Changing spatio-temporal trends of heat wave and severe heat wave events over India: an emerging health hazard. *Int. J. Climatol.* **41**, E1831–E1845 (2021).
8. Panda, D. K., AghaKouchak, A. & Ambast, S. K. Increasing heat waves and warm spells in India, observed from a multiaspect framework. *J. Geophys. Res. Atmos.* **122**, 3837–3858 (2017).
9. Koteswara Rao, K. et al. Projections of heat stress and associated work performance over India in response to global warming. *Sci. Rep.* **10**, 16675 (2020).
10. Pai, D. S., NAIR, S. & Ramanathan, A. N. Long term climatology and trends of heat waves over India during the recent 50 years (1961-2010). *Mausam* **64**, 585–604 (2013).
11. Kyaw, A. K., Hamed, M. M., Kamruzzaman, M. & Shahid, S. Spatiotemporal changes in population exposure to heat stress in South Asia. *Sustain Cities Soc.* **93**, 104544 (2023).
12. Sharma, A., Andhikaputra, G. & Wang, Y. C. Heatwaves in South Asia: characterization, consequences on human health, and adaptation strategies. *Atmosphere* **13**, 734 (2022).
13. Byers, E. et al. Global exposure and vulnerability to multi-sector development and climate change hotspots. *Environ. Res. Lett.* **13**, 055012 (2018).
14. Saeed, F., Schleussner, C. & Ashfaq, M. Deadly heat stress to become commonplace across South Asia already at 1.5 C of global warming. *Geophys. Res. Lett.* **48**, e2020GL091191 (2021).
15. Tucker, J. et al. Social vulnerability in three high-poverty climate change hot spots: what does the climate change literature tell us? *Reg. Environ. Chang.* **15**, 783–800 (2015).
16. Zhang, H. et al. Unequal urban heat burdens impede climate justice and equity goals. *Innovation* **4**, 100488 (2023).

17. Zhao, Q. et al. Global, regional, and national burden of mortality associated with non-optimal ambient temperatures from 2000 to 2019: a three-stage modelling study. *Lancet Planet Health* **5**, e415–e425 (2021).

18. Hess, J. J. et al. Building resilience to climate change: pilot evaluation of the impact of India's first heat action plan on all-cause mortality. *J. Environ. Public Health* **2018**, 7973519 (2018).

19. ESCAP UN. Disasters in Asia and the Pacific: 2015 year in review. http://www.unescap.org/sites/default/files/2015_Year%20in%20Review_final_PDF_1.pdf. Accessed 24 Feb 2018.

20. Saikawa, E. et al. Garbage burning in South Asia: how important is it to regional air quality? *Environ. Sci. Technol.* **54**, 9928–9938 (2020).

21. Goyal, M. K., Singh, S. & Jain, V. Heat waves characteristics intensification across Indian smart cities. *Sci. Rep.* **13**, 14786 (2023).

22. Mishra, V., Thirumalai, K., Singh, D. & Aadhar, S. Future exacerbation of hot and dry summer monsoon extremes in India. *NPJ Clim. Atmos. Sci.* **3**, 10 (2020).

23. Sherwood, S. C. et al. Relative humidity changes in a warmer climate. *J. Geophys. Res. Atmos.* **115**, D09104 (2010).

24. Ivancic, T. J. & Shaw, S. B. A US-based analysis of the ability of the Clausius-Clapeyron relationship to explain changes in extreme rainfall with changing temperature. *J. Geophys. Res. Atmos.* **121**, 3066–3078 (2016).

25. Martinkova, M. & Kysely, J. Overview of observed Clausius-Clapeyron scaling of extreme precipitation in midlatitudes. *Atmosphere* **11**, 786 (2020).

26. Bazett, H. C. Physiological responses to heat. *Physiol. Rev.* **7**, 531–599 (1927).

27. Sawka, M. N. et al. *Physiologic systems and their responses to conditions of heat and cold.* In: Farrell PA, Joyner MJ, Caiozzo VJ, editors. ACSM's advanced exercise physiology. Baltimore: Lippincott Williams & Wilkins; 2012. p. 567–602.

28. Asayama, M. Guideline for the prevention of heat disorder in Japan. *Glob. Environ. Res.* **13**, 19–25 (2009).

29. Blazejczyk, K., Epstein, Y., Jendritzky, G., Staiger, H. & Tinz, B. Comparison of UTCI to selected thermal indices. *Int. J. Biometeorol.* **56**, 515–535 (2012).

30. Kong, Q., Ge, Q., Xi, J. & Zheng, J. Human-biometeorological assessment of increasing summertime extreme heat events in Shanghai, China during 1973–2015. *Theor. Appl. Climatol.* **130**, 1055–1064 (2017).

31. Lim, Y. H. et al. Estimation of heat-related deaths during heat wave episodes in South Korea (2006–2017). *Int. J. Biometeorol.* **63**, 1621–1629 (2019).

32. Dunne, J. P., Stouffer, R. J. & John, J. G. Reductions in labour capacity from heat stress under climate warming. *Nat. Clim. Chang.* **3**, 563–566 (2013).

33. Wang, S. W., Lee, W. K. & Son, Y. An assessment of climate change impacts and adaptation in South Asian agriculture. *Int. J. Clim. Chang. Strateg. Manag.* **9**, 517–534 (2017).

34. Ullah, S. et al. Future population exposure to daytime and nighttime heat waves in South Asia. *Earths Future* **10**, e2021EF002511 (2022).

35. Tuholske, C. et al. Global urban population exposure to extreme heat. *Proc. Natl Acad. Sci. USA* **118**, e2024792118 (2021).

36. Ullah, I. et al. Projected changes in socioeconomic exposure to heatwaves in South Asia under changing climate. *Earths Future* **10**, e2021EF002240 (2022).

37. Ullah, I. et al. Future amplification of multivariate risk of compound drought and heatwave events on South ASIAN population. *Earths Future* **11**, e2023EF003688 (2023).

38. Ullah, I. et al. Spatiotemporal characteristics of meteorological drought variability and trends (1981–2020) over South Asia and the associated large-scale circulation patterns. *Clim. Dyn.* **60**, 2261–2284 (2023).

39. Sein, Z. M. M. et al. Recent variability of sub-seasonal monsoon precipitation and its potential drivers in Myanmar using in-situ observation during 1981–2020. *Int. J. Climatol.* **42**, 3341–3359 (2022).

40. Hersbach, H. et al. The ERA5 global reanalysis. *Q. J. R. Meteorol. Soc.* **146**, 1999–2049 (2020).

41. Brimicombe, C. et al. Wet Bulb Globe temperature: indicating extreme heat risk on a global grid. *Geohealth* **7**, e2022GH000701 (2023).

42. Coco, A. et al. Criteria for a recommended standard: occupational exposure to heat and hot environments Department of Health and Human Services, Centers for Disease Control and Prevention. National Institute for Occupational Safety and Health (2016). https://www.elcosh.org/record/document/3998/d001392.pdf.

43. Jézéquel, A., Yiou, P. & Radanovics, S. Role of circulation in European heatwaves using flow analogues. *Clim. Dyn.* **50**, 1145–1159 (2018).

44. Ye, Y. & Qian, C. Conditional attribution of climate change and atmospheric circulation contributing to the record-breaking precipitation and temperature event of summer 2020 in southern China. *Environ. Res. Lett.* **16**, 044058 (2021).

45. Dally, M. et al. Wet Bulb Globe Temperature and recorded occupational injury rates among sugarcane harvesters in Southwest Guatemala. *Int. J. Environ. Res. Public Health* **17**, 8195 (2020).

46. Qian, C., Ye, Y., Bevacqua, E. & Zscheischler, J. Human influences on spatially compounding flooding and heatwave events in China and future increasing risks. *Weather Clim. Extrem.* **42**, 100616 (2023).

47. Eyring, V. et al. Overview of the Coupled Model Intercomparison Project Phase 6 (CMIP6) experimental design and organization. *Geosci. Model Dev.* **9**, 1937–1958 (2016).

48. Gao J. *Downscaling Global Spatial Population Projections from 1/8-Degree to 1-Km Grid Cells.*; https://doi.org/10.5065/D60Z721H (2017)

49. American College of Sports Medicine. Prevention of thermal injuries during distance running. *Phys. Sportsmed.* 12, 43–51 (1984).

50. Liljegren, J. C., Carhart, R. A., Lawday, P., Tschopp, S. & Sharp, R. Modeling the wet bulb globe temperature using standard meteorological measurements. *J. Occup. Environ. Hyg.* **5**, 645–655 (2008).

51. Stull, R. Wet-bulb temperature from relative humidity and air temperature. *J. Appl. Meteorol. Climatol.* **50**, 2267–2269 (2011).

52. Lemke, B. & Kjellstrom, T. Calculating workplace WBGT from meteorological data: a tool for climate change assessment. *Ind. Health* **50**, 267–278 (2012).

53. Yiou, P., Vautard, R., Naveau, P. & Cassou, C. Inconsistency between atmospheric dynamics and temperatures during the exceptional 2006/2007 fall/winter and recent warming in Europe. *Geophys. Res. Lett.* **34**, L21808 (2007).

54. Zhang, X. et al. Increased impact of heat domes on 2021-like heat extremes in North America under global warming. *Nat. Commun.* **14**, 1690 (2023).

55. Jones, B. et al. Future population exposure to US heat extremes. *Nat. Clim. Chang.* **5**, 652–655 (2015).

56. Xie, W., Zhou, B., Han, Z. & Xu, Y. Substantial increase in daytime-nighttime compound heat waves and associated population exposure in China projected by the CMIP6 multimodel ensemble. *Environ. Res. Lett.* **17**, 045007 (2022).

57. Zhang, G. et al. Increasing heatwave with associated population and GDP exposure in North China. *Int. J. Climatol.* **43**, 4716–4732 (2023).

Acknowledgements

Competing interests

The authors declare no competing interests.

Additional information

Supplementary information The online version contains supplementary material available at https://doi.org/10.1038/s41612-024-00764-5.

Correspondence and requests for materials should be addressed to Deliang Chen.

Reprints and permissions information is available at http://www.nature.com/reprints

Publisher's note Springer Nature remains neutral with regard to jurisdictional claims in published maps and institutional affiliations.